

First-principles study of the quasi-one-dimensional organic-inorganic hybrid perovskites (MV)Al₃Cl₂ (MV = methylviologen; A = Bi, Sb)

Chao Wang,¹ Yunlin Lei²,^{*} Winnie Wong-Ng,³ Qiang Gu,¹ Xingxing Wu,¹ Wei Zhou,¹ Shouyu Wang,^{2,*} and Weifang Liu^{1,†}

¹Tianjin Key Laboratory of Low Dimensional Materials Physics and Preparing Technology, School of Science, Tianjin University, Tianjin 300072, China

²College of Physics and Material Science, Tianjin Normal University, Tianjin 300074, China

³Materials Measurement Science Division, National Institute of Standards and Technology, Gaithersburg, Maryland 20899, USA



(Received 20 March 2021; revised 11 July 2021; accepted 6 August 2021; published 20 August 2021)

Many ferroelectric (FE) organic-inorganic hybrid perovskites (OIHPs) show great promise in the fields of photovoltaic cells and information memory devices. We systematically investigated the FE, optical, and electric properties of quasi-one-dimensional OIHPs (MV)Al₃Cl₂ (MV = methylviologen, A = Bi, Sb) using density functional theory calculations. The FE polarization mechanism of (MV)Al₃Cl₂ mainly originates from octahedral distortion along the direction of octahedral chains with the *p-p* coupling of A³⁺ cations and I⁻ anions. Due to the loosely coupled FE chains, (MV)BiI₃Cl₂ and (MV)SbI₃Cl₂ possess a relatively low energy barrier of polarization switching at the 180° reversal of the FE polarization. The estimated upper limit memory densities of 14.9 and 15.0 Tb/cm² for (MV)BiI₃Cl₂ and (MV)SbI₃Cl₂, respectively, hold promise to be applied to high-density FE memory devices. The strong anisotropic optical absorption of (MV)Al₃Cl₂ is in the visible light region, and its estimated maximum power conversion efficiencies are >23%. The high anisotropic carrier mobility in (MV)Al₃Cl₂ enhances the separation of electron-hole pairs. Both (MV)BiI₃Cl₂ and (MV)SbI₃Cl₂ possess positive piezoelectric effect; therefore, strain design is an effective approach to enhance power conversion efficiency and carrier mobility of (MV)Al₃Cl₂, leading to experimental design of FE photovoltaic cell.

DOI: [10.1103/PhysRevB.104.075138](https://doi.org/10.1103/PhysRevB.104.075138)

I. INTRODUCTION

In recent years, interest in organic-inorganic hybrid perovskites (OIHP) has intensified in the fields of photovoltaic cells and information storage due to their simple room-temperature manufacturing process, adjustable band gap width, strong optical absorption, and excellent electronic transport properties [1–9]. Taking solar photovoltaics as an example, the photoelectric conversion efficiency of CH₃NH₃PbI₃ built-in batteries in the last decade has increased from <4 to >25% [10,11]. More importantly, using the ferroelectric (FE) polarization of CH₃NH₃PbI₃ to control the generation and transport of carriers helps to improve the photoelectric conversion capability of solar cells. In addition, FE OIHPs with outstanding properties have been applied successfully to memristors [4]. For example, Yoo *et al.* [12] reported the development of resistive random access memory devices using CH₃NH₃PbI_{3-x}Cl_x, and CH₃NH₃PbI_{3-x}Cl_x with active metals as top electrodes exhibited excellent memristive properties. However, the toxic Pb element in CH₃NH₃PbI₃ is environmentally unfriendly, which hinders its large-scale industrial production in photovoltaic cells and memristors. Therefore, it is an important research topic in the fields of photovoltaic cells and memristors to search for Pb-free OIHP materials.

Recently, many researchers focused their efforts on searching for excellent electrical reliability and polarization retention properties in OIHP (MV)Al₃Cl₂ (MV = methylviologen, A = Bi, Sb) [13–16]. Leblanc *et al.* [13] reported that (MV)BiI₃Cl₂ was successfully synthesized by the solvothermal method at 150°C, and the material possesses excellent stability in air. The robust spontaneous polarization (*P*_s > 0.15 C/m²) of (MV)BiI₃Cl₂ was clearly shown by the hysteresis loop at room temperature [13]. Our group further investigated the ultralow electric field-driven dielectric tunability in (MV)BiI₃Cl₂ [14], which is a promising candidate for switching devices and memory storage. (MV)BiI₃Cl₂ with strong optical absorption was used for photodegradation of wastewater [16]. Leblanc *et al.* [15] reported that (MV)SbI₃Cl₂, like (MV)BiI₃Cl₂ with a FE polarization transition, is also a potential FE material. In short, FE (MV)BiI₃Cl₂ and (MV)SbI₃Cl₂ with strong optical absorption and robust FE properties appear to be potential candidates for FE photovoltaic cells and memory applications. However, the FE mechanical and photoelectric properties of (MV)BiI₃Cl₂ and (MV)SbI₃Cl₂ are still unclear and need to be further investigated.

FE materials often exhibit piezoelectric effects. The spontaneous polarization and optical properties of FE materials can generally be affected by crystal structure distortions via different experimental methods including annealing [17], doping with different elements [18], and applying electric fields [19]. Similarly, strain engineering was widely used to enhance the FE property of inorganic perovskites such as BaTiO₃,

*Corresponding author: shouyu.wang@yahoo.com

†Corresponding author: wfliu@tju.edu.cn

SrTiO₃, and CaTiO₃ [20]. Recent research showed that strain engineering can be employed to substantially control FE polarization of OIHPs [21]. However, there are very few studies on improving FE properties of quasi-one-dimensional (1D) materials (MV)Al₃Cl₂ by applying strain engineering.

In this paper, the mechanical characteristics, FE mechanism, optical properties, and carrier mobility of (MV)Al₃Cl₂ (*A* = Bi, Sb) are systematically investigated with first-principles calculations. The calculated results indicate that (MV)Al₃Cl₂ possesses mechanical stability according to the Born stability criteria [22]. The robust FE polarization along the *c* direction was originated from atom displacements including distorted octahedra and dynamic MV molecules. The relatively low energy barrier of polarization reversal is beneficial to the applications of (MV)BiI₃Cl₂ and (MV)SbI₃Cl₂ in FE memory devices. The spontaneous polarization of (MV)Al₃Cl₂ increases with increasing stretching, showing positive piezoelectric response. The optical absorption coefficient and carrier mobility of (MV)Al₃Cl₂ can also be effectively tuned by strain engineering. Through this technique, it is possible that (MV)BiI₃Cl₂ and (MV)SbI₃Cl₂ possess robust FE polarization, strong light absorption, and high carrier mobility, which are critical properties for materials to be potential candidates for FE photovoltaic and high-density memory applications.

II. CALCULATION DETAILS

All calculations in this paper were performed via the projector-augmented-wave method with the Vienna *ab initio* Simulation Package (VASP) based on density functional theory (DFT) [23,24]. For the exchange correlation, we have adopted the generalized gradient approximation (GGA) parameterized by Perdew-Burke-Ernzerhof (PBE) [25]. As we all know, the GGA function ignores the Hartree-Fock precise exchange part, resulting in the underestimation of the band gap of semiconductors and insulators. Thus, the Heyde-Scuseria-Ernzerhof (HSE06) hybrid functional was adopted to calculate the electronic structures [26,27]. The electronic states are expanded using plane wave up to a cutoff energy of 500 eV. The Brillouin zone was sampled with $3 \times 3 \times 3$ and $4 \times 4 \times 4$ Monkhorst-Pack *k*-points grids for geometry optimization and self-consistent calculations, respectively. For total energy calculations, the convergence was set at $<10 \mu\text{eV}/\text{atom}$. All atomic coordinates and lattice constants were optimized until all residual forces were $<0.01 \text{ eV}/\text{\AA}$. The FE polarization was calculated with the modern theory of polarization based on the Berry phase approach [28]. The activation barrier of polarization switching pathways was obtained with the nudged elastic band method [29]. The symmetry analysis was used with the Bilbao Crystallographic Server [30]. The spin-orbit coupling effect was considered because of the heavy metals Sb and Bi. The optical absorption spectra are described by the complex dielectric function, i.e., $\varepsilon(\omega) = \varepsilon_1(\omega) + i\varepsilon_2(\omega)$. Based on the dielectric function of (MV)Al₃Cl₂, the absorption coefficient $\alpha(\omega)$ is given by the following equation [31]:

$$\alpha(\omega) = \frac{\sqrt{2}\omega\sqrt{\sqrt{\varepsilon_1(\omega)^2 + \varepsilon_2(\omega)^2} - \varepsilon_1(\omega)}}{c}, \quad (1)$$

where $\varepsilon_1(\omega)$ and $\varepsilon_2(\omega)$ are the real and imaginary part of the dielectric function, respectively. Here, ω is the photon frequency, and *c* is the speed of light.

For the OIHPs as a single-junction solar cell, the maximum short-circuit current (J_{sc}), open-circuit voltage (V_{oc}), and maximum power conversion efficiency (η) were calculated based on the material band gap with following equations [32–34]:

$$J_{sc} = e \int_{E_g}^{\infty} \frac{S(E)}{E} dE, \quad (2)$$

$$V_{oc} = (E_g - E_{loss})/e, \quad (3)$$

$$\eta(E_g) = \frac{FF \times J_{sc} \times V_{oc}}{P_{sum}}, \quad (4)$$

$$P_{sum} = \int_0^{\infty} S(E) dE, \quad (5)$$

where *e*, *E*, E_g , $S(E)$, E_{loss} , FF, and P_{sum} stand for the electric charge, the incident photon energy, the material band gap, the power of solar radiation per unit area, the loss-in-potential, fill factor, and the total incident power, respectively. Importantly, the maximum short-circuit current assumes that only photons with an energy above the band gap can generate electron-hole pairs with a quantum efficiency of 100% [35]. We selected two calculated parameters 0.5 and 0.7 eV for E_{loss} and 80% for FF, respectively, relying on the calculated experience values of organic-inorganic hybrid materials reported by many research groups [34,36]. The P_{sum} is calculated based on AM 1.5G solar radiation spectra provided by the National Renewable Energy Laboratory [37].

III. RESULTS AND DISCUSSION

A. Geometric structure

The side and top views of the optimized FE phase (No. 104, *P4nc*) of (MV)Al₃Cl₂ (*A* = Bi, Sb) are shown in Figs. 1(a) and 1(b), respectively. The crystal structures of (MV)Al₃Cl₂ are composed of MV organic molecules and Al₃Cl₂ inorganic octahedral chains, where two different anions I and Cl in the equatorial plane form alternating Al₃ and AlCl₂ octahedrons in a chain parallel to the *c* axis. In fact, the isolated inorganic octahedral chains are separated by large planar organic molecules. According to Goldschmidt's rule for large organic molecules [38,39], the OIHPs tend to form low-dimensional structures. Due to the similarity to a macromolecule, (MV)Al₃Cl₂ with long inorganic chains can be treated as a quasi-1D OIHP structure. Because of the dispersive force in the OIHP structures, the calculated parameter *c* of (MV)Al₃Cl₂ (Table S1 in the Supplemental Material (SM) [40]) is overestimated with the PBE method as compared with the experimental results [13,15]. We adopted three well-known corrections to the van der Waals forces, namely, the PBE-D2 [41], PBE-D3 [42], and PBE-optB86b [43] methods, to optimize the structures, as shown in Table S1 in the SM [40]. The calculated results indicate that optimized structure parameters with the PBE-D3 method agree better with experimental results, as shown in Table I. Thus, this method was adopted for the following calculations.

It is well known that, in a structure possessing a polar space group, the centers of positive and negative charges no longer

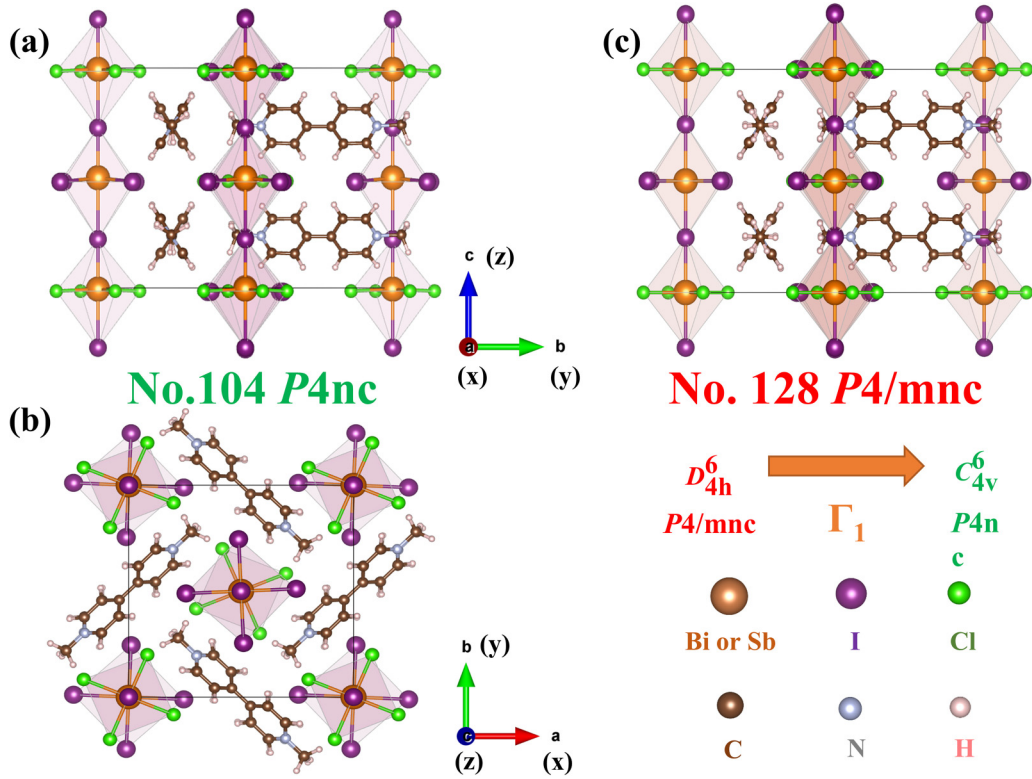


FIG. 1. (a) Side and (b) top views of ferroelectric (FE) phases $(MV)Al_3Cl_2$ (No. 104, $P4nc$), which are composed of Al_3Cl_2 octahedral chains and MV molecules (MV = methylviologen, $A = Bi, Sb$). The brown, purple, green, light brown, silver, and pink spheres represent Bi or Sb, I, Cl, C, N, and H atoms, respectively. (c) Side view of the paraelectric (PE) phase $(MV)Al_3Cl_2$ (No. 128, $P4/mnc$). The phase transition (with Γ_1 soft model) to the FE phase (C_{4v}^6) originated from destroying the c -axis mirror symmetry of the PE phase (D_{4h}^6).

coincide, suggesting that spontaneous polarization is most likely to occur, and the material can usually be deemed as FE. The FE phases of $(MV)Al_3Cl_2$ are of noncentrosymmetric polar space group $P4nc$ (C_{4v}^6 , No. 104). Using the symmetry software PSEUDOSYMMETRY [44], the paraelectric (PE) phase was confirmed to have the centrosymmetric space group of $P4/mnc$ (No. 128), as shown in Fig. 1(c), where all A ions are at the center of the octahedral chains Al_3Cl_2 and organic molecules MV are located in the center between adjacent Al_3Cl_2 octahedrons. The symmetrical atomic displacement of inorganic octahedral chains along the c axis indicates that the equivalent positive and negative charge centers are parallel to the c axis and form zero polarization. In addition, the centrosymmetric phase of $P4/mnc$ is also verified in the experimental report [45]. According to the polar spatial symmetry of the FE phase ($P4nc$), the theoretical analysis of the space

group with the AMPLIMODES software [46,47] showed that the atomic distortion mode is the Γ_1^- mode and that the polar axis is only along the c direction. That is, the mirror symmetry along the c axis of the PE phase is destroyed to construct the uniaxial polarization.

B. The FE mechanism

In OIHP $(MV)Al_3Cl_2$, the obvious characteristic difference between ferroelectricity and paraelectricity is the octahedral distortion, where the A^{3+} cations in the Al_3 and $AlCl_2$ structures are off-center in the FE phase. In addition, the nonpolar MV organic molecules slightly shift along the c direction as compared with the PE phase. However, the contribution of inorganic and organic structural displacements to the FE polarization is still unclear. To clarify this FE mechanism, the total contribution to FE polarization of $(MV)Al_3Cl_2$ is

TABLE I. Physical properties of FE phases (space group: $P4nc$) in $(MV)BiI_3Cl_2$ and $(MV)SbI_3Cl_2$ were obtained by DFT calculations using the D3 method (PBE-D3) compared with experimental (Exp.) results data including the lattice constants $a = b$ and c (\AA), volume constant V (\AA^3), FE polarization P ($\mu\text{C}/\text{cm}^2$), α [$10^{-2} \text{ meV}/(\mu\text{C}/\text{cm}^2)^2$], β [$10^{-4} \text{ meV}/(\mu\text{C}/\text{cm}^2)^4$], and coercive field E_c (kV/cm). The decomposition of the piezoelectric response contributions ($\partial p/V_0 \partial \epsilon$) is given in Eq. (12) ($\mu\text{C}/\text{cm}^2$).

Material	Method	$a = b$	c	V	P	α	β	E_c	$\frac{1}{V_0} \frac{\partial p}{\partial \epsilon}$
$(MV)BiI_3Cl_2$	PBE-D3	12.34	12.89	1964.94	5.93	-3.84	0.09	1270	59.93
$P4nc$	Exp. [13]	12.53	12.65	1985.53	15	-	-	0.1-0.2	-
$(MV)SbI_3Cl_2$	PBE-D3	12.29	12.85	1942.49	6.64	-4.61	0.10	1880	31.54
$P4nc$	Exp. [15]	12.51	12.58	1968.58	-	-	-	-	-

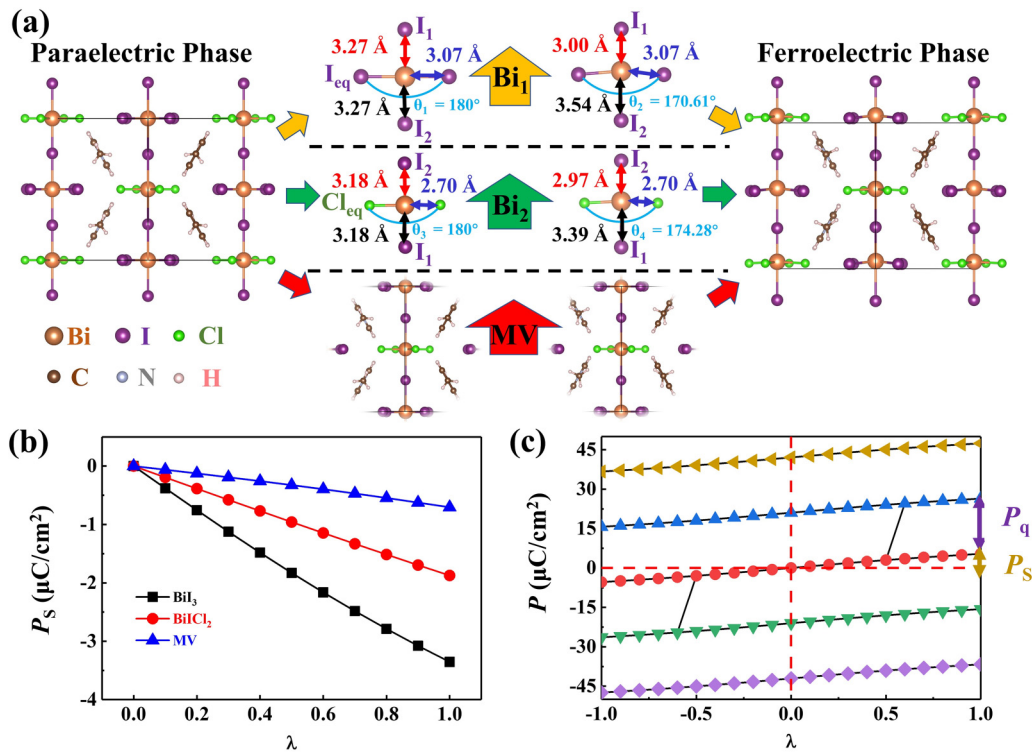


FIG. 2. (a) From paraelectric (PE) to ferroelectric (FE) phase, (MV)Bi₃Cl₂ structure is divided into three parts: BiI₃, BiI₂Cl₂, and MV, and the change of bond length and bond angle are also shown in detail. (b) The change of FE polarization of MV molecules, BiI₃, and BiI₂Cl₂ octahedrons in (MV)Bi₃Cl₂ with the amplitude of the distortion mode (λ) between nonpolar and polar phases, where the $\lambda = 0$ and 1 stand for the PE and FE phases, respectively. (c) The change in polarization P along a path from the original FE structure ($\lambda = 1$) through the centrosymmetric PE structure ($\lambda = 0$) to the inverted FE structure ($\lambda = -1$). The possible values of P for fixed distortion differ by multiples of the polarization quantum (P_q) 21.03 $\mu\text{C}/\text{cm}^2$ for $2ec/V$, where e is the charge of the electron, c is the lattice constant along the c direction, and V is the volume of unit cell.

divided into three parts: (1) The FE polarization P_{Al_3} induced by displacement polarization of A^{3+} cations and I^- anions in the Al_3 octahedrons; (2) The FE polarization P_{AlCl_2} induced by displacement polarization of A^{3+} cations and I^- (Cl^-) anions in the AlCl_2 octahedrons; (3) The FE polarization P_{MV} induced by displacement polarization of the MV molecules. Contributions of three different polarization components for (MV)Bi₃Cl₂ and (MV)SbI₃Cl₂ will be discussed as follows.

Due to the similar structure between (MV)Bi₃Cl₂ and (MV)SbI₃Cl₂, (MV)Bi₃Cl₂ was selected to analyze for the three components of FE polarization. First, in the BiI₃ octahedron [Fig. 2(a)], the Bi³⁺ cations and the I⁻ anions carry positive and negative charges, respectively. For the PE phases, the Bi³⁺ cations are located in the octahedron center of the I⁻ anions. The equivalent positive charge center of Bi³⁺ and the equivalent negative charge center of I⁻ coincide with each other, resulting in zero polarization. For the FE phases, the Bi³⁺ cations with positive charge are off-center of the I⁻ octahedron with negative charge, resulting in two different bond angles ($I_{\text{eq}}\text{-Bi}_1\text{-I}_{\text{eq}}$) and bond lengths ($\text{Bi}_1\text{-I}_1$) at the equatorial plane. Here, we calculated the polarization process as a series of phase transition. The amplitude of the distortion mode λ (normalized to one parameter) was introduced as displacement of cations and anions, where $\lambda = 0$ and 1 represent PE and FE phases, respectively, as shown in Fig. 2(b). During the phase transition process, the bond angle $I_{\text{eq}}\text{-Bi}_1\text{-I}_{\text{eq}}$ changes from 180° (PE) to 170.61° (FE), and the bond length of Bi₁-I₁

is shortened from 3.27 to 3.00 Å. The bond length of Bi₁-I_{eq} (3.07 Å) at the equatorial plane is nearly unchanged in the FE and PE phases. It is further confirmed that the direction of FE polarization is only along the c direction. The calculated polarization of the Al_3 octahedron is mostly linear with the amplitude of the distortion mode λ . The continuous variation of the calculated polarization curve eliminates the possible influence of polarization quantum due to the Born-von Karman periodic boundary conditions [48]. The FE polarization of the BiI₃ octahedron (P_{BiI_3}) increases from 0 to 3.35 $\mu\text{C}/\text{cm}^2$ along the c axis, which is a large value compared with many other OIHP materials [49,50]. The FE polarization P_{BiI_3} originates from the displacement between the positive charge of octahedral Bi³⁺ cations and the negative charge of I⁻ anions.

The FE polarization contribution of BiI₂Cl₂ octahedrons ($P_{\text{BiI}_2\text{Cl}_2}$) with different I and Cl anions was analyzed next. Because the electronegativity of the Cl atom (3.16) in the BiI₂Cl₂ octahedrons of the PE phase is much greater than that of the I atom (2.66), the bond length between the Bi cation and Cl anion on the equatorial plane of the BiI₂Cl₂ octahedron ($\text{Bi}_2\text{-Cl}_{\text{eq}}$: 2.70 Å) is evidently smaller than that between Bi and I on the equatorial plane of the BiI₃ octahedron ($\text{Bi}_1\text{-I}_{\text{eq}}$: 3.07 Å). The bond length of Bi₂-I₂ (3.18 Å), on the other hand, is shorter than that of Bi₁-I₁ (3.27 Å). The Cl anions with strong electronegativity almost hinder the movement of the Bi cations along the c direction as compared with the displacement of Bi cations in the BiI₃ octahedron. Results of transition

phase calculations showed that the bond angle $\text{Cl}_{\text{eq}}\text{-Bi}_2\text{-Cl}_{\text{eq}}$ changes from 180° (PE) to 174.28° (FE), which is slightly larger than that of $\text{I}_{\text{eq}}\text{-Bi}_1\text{-I}_{\text{eq}}$ (170.61°). The displacement of Bi_2 atoms in the BiICl_2 octahedron is indeed smaller than that of Bi_1 atoms in the BiI_3 octahedron. Thus, in the normal displacement paths, P_{BiICl_2} ($1.87 \mu\text{C}/\text{cm}^2$) is smaller than P_{BiI_3} [as shown in Fig. 2(b)], indicating that the main contribution to FE polarization is the displacement polarization of Bi_1 atoms. The displacement polarization of the SbI_3Cl_2 inorganic octahedron is slightly larger than that of the BiI_3Cl_2 structure due to the small volume of $(\text{MV})\text{SbI}_3\text{Cl}_2$ (Table I). In the AlI_3 and AlCl_2 octahedrons, displacements of the Bi^{3+} or Sb^{3+} centers introduce FE polarization, like the FE mechanism in traditional perovskites, for example, BaTiO_3 [51–53].

The organic molecule MV, an integral part of the OIHP structure, is expected to have a nonnegligible contribution to the total FE polarization. The MV molecule can be seen as positively charged molecules relative to the negatively charged BiI_3Cl_2 inorganic octahedron. During the transition from PE to FE phase, the displacement pathway of all MV is along the c axis, which is different from the FE mechanism of small organic molecule rotation (i.e., in OIHP $\text{CH}_3\text{NH}_3\text{PbI}_3$) [54]. As shown in Figs. 2(b) and S1(a) in the SM [40], the calculated MV polarization (P_{MV}) along the c axis increases from 0 to $0.71 \mu\text{C}/\text{cm}^2$ and to $0.83 \mu\text{C}/\text{cm}^2$ for $(\text{MV})\text{BiI}_3\text{Cl}_2$ and $(\text{MV})\text{SbI}_3\text{Cl}_2$, respectively. This result reveals that the displacement polarization of MV molecules has a small contribution to FE OIHP materials, which agrees well with previous papers on FE polarization of OIHPs, for example, $(\text{MV})\text{BiBr}_5$ [55] and $(\text{C}_3\text{N}_2\text{H}_5)_2\text{SbCl}_5$ [56].

The mechanism of OIHP ferroelectricity will be discussed based on the analysis of the above three cases. Due to the symmetry characteristics of the $4mm$ polar point group of the tetragonal system, $(\text{MV})\text{AlI}_3\text{Cl}_2$ with FE polarization is unidirectional and is along the quasi-1D inorganic chains. The FE polarization of $(\text{MV})\text{AlI}_3\text{Cl}_2$ is mainly contributed by the relative displacement of the AlI_3Cl_2 octahedron, which contains two types of octahedrons AlI_3 and AlCl_2 , where the displacement of Bi^{3+} or Sb^{3+} centers mainly induce FE polarization. Moreover, the displacement of organic molecules relative to inorganic chains induces only small FE polarization. Accounting for the contributions from the inorganic component and organic molecules, the total FE polarization P_{total} is given by

$$P_{\text{total}} = P_{\text{AlI}_3} + P_{\text{AlCl}_2} + P_{\text{MV}}. \quad (6)$$

The $(\text{MV})\text{BiI}_3\text{Cl}_2$ with robust spontaneous polarization of $5.93 \mu\text{C}/\text{cm}^2$ is lower than experimental results ($P_S > 15 \mu\text{C}/\text{m}^2$) [13]. The reason for lower spontaneous polarization may be due to the small displacement of the organic molecules MV. In addition, the error range between experiments and theoretical calculations is $\sim 50\%$ when the spontaneous polarization of material was measured $> 10 \mu\text{C}/\text{cm}^2$ [57]. Due to the Born–von Karman periodic boundary conditions [48], there is an ambiguity in the choice of unit cell, and overall polarization may be significantly affected by an integer multiple of the polarization quantum $P_q = eR/V$, where e is the charge of the electron, R is a lattice vector in the direction of P , and V is the volume of the unit cell [58]. The P_q of $(\text{MV})\text{BiI}_3\text{Cl}_2$ and $(\text{MV})\text{SbI}_3\text{Cl}_2$ is 21.03 and $21.20 \mu\text{C}/\text{cm}^2$, respectively. The spontaneous

polarization was calculated with Eq. (7):

$$P_S = P_{\text{FS}} + nP_q - P_{\text{IS}}, \quad (7)$$

where n , P_{FS} , and P_{IS} represent an integer and the polarization of the final and initial states in the path from PE to FE state, respectively. The P_S of $(\text{MV})\text{BiI}_3\text{Cl}_2$ and $(\text{MV})\text{SbI}_3\text{Cl}_2$ are 5.93 and $6.64 \mu\text{C}/\text{cm}^2$, as shown in Figs. 2(c) and S1(b) in the SM [40], respectively. The P_S of $(\text{MV})\text{SbI}_3\text{Cl}_2$ is comparable with other OIHP ferroelectricity such as FASnI_3 ($8.41 \mu\text{C}/\text{cm}^2$) [59] and $(\text{PFBA})_2\text{PbBr}_4$ ($4.2 \mu\text{C}/\text{cm}^2$) [60]. The difference upon varied k -points is subtle, indicating that the convergence of polarization meets the criterion, as shown in Table S2 in the SM [40]. There is the three- or fivefold difference between the number of polarized quantum and the calculated spontaneous polarization, which is like the series of reported results in other FE inorganic perovskite materials, such as BaTiO_3 ($P_q = 2.036 \text{ C}/\text{m}^2$, $P_S = 0.351 \text{ C}/\text{m}^2$) and KNbO_3 ($P_q = 1.002 \text{ C}/\text{m}^2$, $P_S = 0.369 \text{ C}/\text{m}^2$) [61].

C. Mechanical switching

The energy barrier of the FE transition of FE materials is important for the coercive field and for determining the material applications in information storage and photovoltaic devices. FE polarization in quasi-1D $(\text{MV})\text{AlI}_3\text{Cl}_2$ should be switchable under an applied electric field. Based on the above analysis that FE polarization mainly originates from the inorganic chains, the 1D FE orders are along the direction of the octahedral chains. The FE polarization switching should be achievable through the direct reversal of the polarization direction by 180° along the c axis. Therefore, the FE or anti-ferroelectric (AFE) phase is confined to be along the polar c axis. We will consider two simple and ideal switching paths for $(\text{MV})\text{BiI}_3\text{Cl}_2$ and $(\text{MV})\text{SbI}_3\text{Cl}_2$: (1) switching all chains together, as shown in Fig. 3(a), and (2) switching only half chains, as shown in Fig. 3(b).

As the off-center A^{3+} cations in both $(\text{MV})\text{BiI}_3\text{Cl}_2$ and $(\text{MV})\text{SbI}_3\text{Cl}_2$ change from PE to FE phase [Figs. 3(c) and 3(d)], a double-well structure was obtained in the energy vs polarization plots (when all chains were switched). The minimum energy refers to the stable FE phase. In the phase transition process, the energy barrier of $(\text{MV})\text{BiI}_3\text{Cl}_2$ ($42 \text{ meV}/\text{f.u.}$) is obviously smaller than that of $(\text{MV})\text{SbI}_3\text{Cl}_2$ ($67 \text{ meV}/\text{f.u.}$). The classical double-well potential curves can be fitted using the Landau-Ginzburg-Devonshire formula [62]:

$$G = \frac{\alpha}{2}P^2 + \frac{\beta}{4}P^4, \quad (8)$$

where G and P are the free energy and FE polarization of the system, respectively. Energy contributions up to the fourth order are necessary to describe the anharmonic double-well potential. The values of the energy coefficients in Eq. (8) are extracted from the DFT calculations, as listed in Table I. Based on the Landau phenomenological phase transition model, to evaluate the process of electric-field-induced polarization switching for $(\text{MV})\text{AlI}_3\text{Cl}_2$, we considered the field aspect and directly simulated the polarization field hysteresis loop. The free energy of $(\text{MV})\text{AlI}_3\text{Cl}_2$ under the c direction

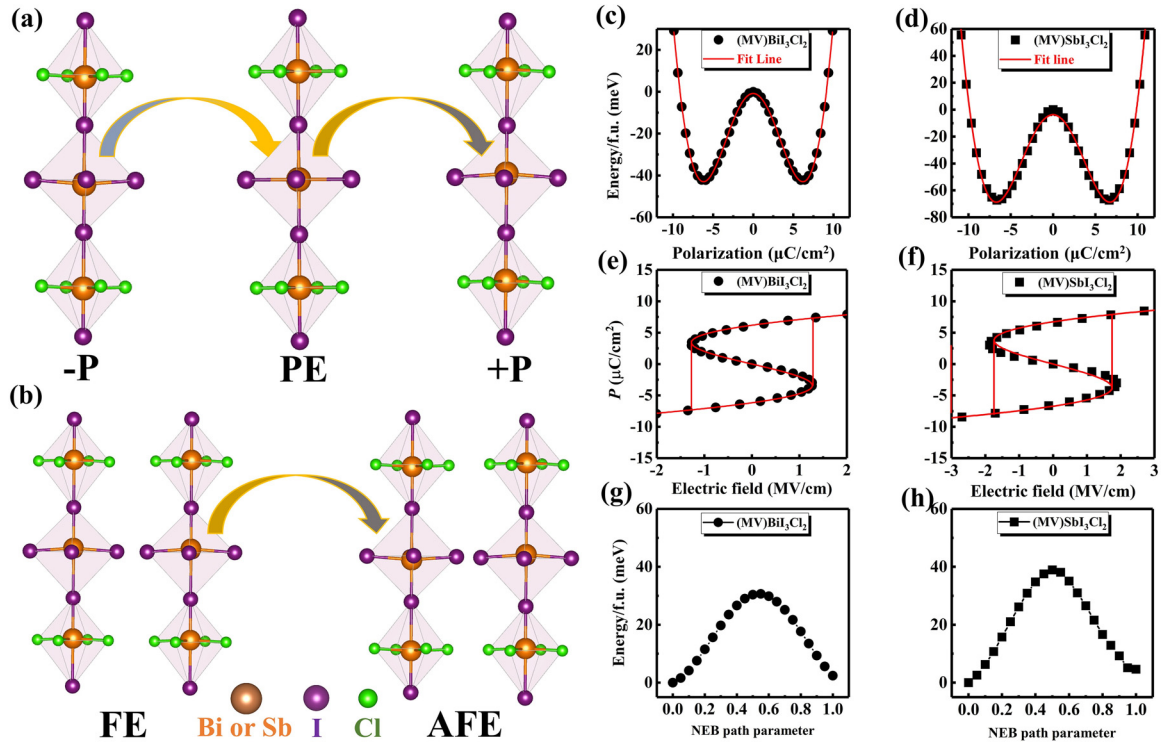


FIG. 3. Simple schematic diagrams of (a) ferroelectric (FE) state inversion and (b) transition from FE to antiferroelectric (AFE) states in $(MV)Al_3Cl_2$ along the direction of octahedral chains. The brown, purple, and green spheres represent Bi or Sb, I, and Cl atoms, respectively. The double well potential of (c) $(MV)Bi_3Cl_2$ and (d) $(MV)Sb_3Cl_2$ along an adiabatic path. The hysteresis loops of (e) $(MV)Bi_3Cl_2$ and (f) $(MV)Sb_3Cl_2$ were inferred by Landau's principle. The nudged elastic band calculation for a minimum energy pathway of (g) $(MV)Bi_3Cl_2$ and (h) $(MV)Sb_3Cl_2$ from FE to AFE phase.

can be expressed as follows [63]:

$$G' = \frac{\alpha}{2}P^2 + \frac{\beta}{4}P^4 - E \cdot P, \quad (9)$$

where E is the electric field. Taking derivatives of both sides of Eq. (9) and setting $dG/dP = 0$, the relationship between applied electric field E and polarization P can be obtained:

$$E = \alpha P + \beta P^3. \quad (10)$$

According to the Eq. (10), FE polarization along the c direction of $(MV)Al_3Cl_2$ is reversible under external electric field, as shown in Figs. 3(e) and 3(f). From the energy barrier of the double well, the coercive fields (E_c) of $(MV)Bi_3Cl_2$ and $(MV)Sb_3Cl_2$ are 1.27 and 1.88 MV/cm, respectively. We found that the larger the potential barrier of polarization reversal, the larger the coercive field. More importantly, the calculated E_c of $(MV)Bi_3Cl_2$ in the hysteresis loop is ~ 4 orders of magnitude larger than the experimentally measured value ($E_c \approx 0.1 - 0.2$ kV/cm at room temperature) [13], which is due to the reason that the polarization conversion process of $(MV)Al_3Cl_2$ was only simulated using one unit cell. This overestimate is typical and is often attributed to an extrinsic effect of defect sites [64]. In fact, the energy barrier for polarization reversal through FE domain wall motion should be much smaller [65]. For example, it was reported that the coercive electric field for FE domain reversal in the lithium salts $LiTaO_3$ and $LiNbO_3$ estimated using the phenomenolog-

ical free energy theory is often several orders of magnitude higher than the results from experimental measurement [64]. Hence, the domain wall motion needs to be further studied experimentally.

When switching only half of the number of chains, we found that the pathway with the lowest activation barrier to reverse the electric polarization goes through an intermediate AFE phase, as shown in Figs. 3(g) and 3(h). The AFE phase is less stable than the FE phase by ~ 2 and 5 meV/f.u. in $(MV)Bi_3Cl_2$ and $(MV)Sb_3Cl_2$, respectively. Although the relative energy of AFE and FE phases is very close, they are separated by a sizeable energy barrier [~ 30 and 38 meV/f.u. for $(MV)Bi_3Cl_2$ and $(MV)Sb_3Cl_2$, respectively]. These values are, however, much lower than the difference energy between PE and FE phases, indicating the easier switching between the AFE and FE phases. Compared with the well-known FE perovskite $LiNbO_3$ with energy barrier of 260 meV [66], $(MV)Al_3Cl_2$ could become a competitive FE material for nonvolatile logic and memory devices with switchable polarizations. When the smallest FE domain in a low-dimensional FE OIHP is treated as a chain, $(MV)Al_3Cl_2$ may function as a potential high-performance FE memory density compared with conventional FE perovskites. Considering each chain to be the minimal memory unit of one bit, the upper limit of theoretical density was estimated as 14.9 and 15.0 Tb/cm² for $(MV)Bi_3Cl_2$ and $(MV)Sb_3Cl_2$, respectively, which is larger than that of $LiNbO_3$ (density of 86.5 Gbit/cm²) [67].

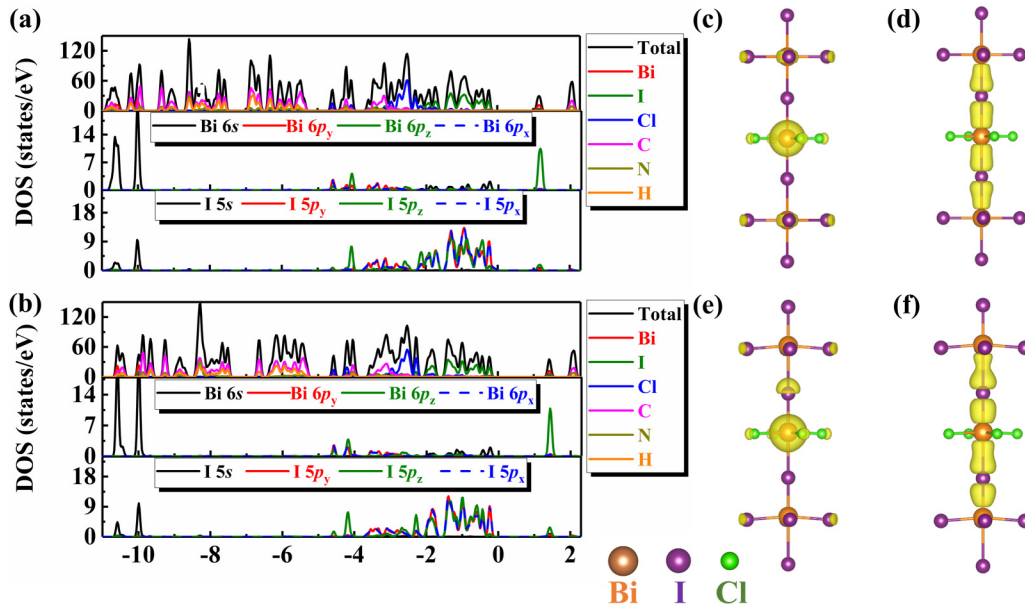


FIG. 4. The atomic total and projected density of states (PDOS) of (a) paraelectric (PE) and (b) ferroelectric (FE) phases in the $(\text{MV})\text{BiI}_3\text{Cl}_2$. The partial charge density of Bi cation with $6s^2$ lone pairs in the (c) PE and (e) FE phases. The partial charge density of p - p coupling between Bi^{3+} and I^- atoms in the (d) PE and (f) FE phases. The value of isosurface is set to be $0.015 \text{ e}/\text{\AA}^3$. The brown, purple, and green spheres represent Bi, I, and Cl atoms, respectively.

D. The electronic performance and light absorption

To understand the electronic structure as a result of phase transition, the total and projected density of states (PDOS) of PE and FE phases of $(\text{MV})\text{BiI}_3\text{Cl}_2$ and $(\text{MV})\text{SbI}_3\text{Cl}_2$ were calculated and shown in Figs. 4 and S2 in the SM [40]. Since the electronic structures of FE $(\text{MV})\text{BiI}_3\text{Cl}_2$ and $(\text{MV})\text{SbI}_3\text{Cl}_2$ are basically similar in Fig. S3 in the SM [40], $(\text{MV})\text{BiI}_3\text{Cl}_2$ was selected for detailed analysis. The FE phase of $(\text{MV})\text{BiI}_3\text{Cl}_2$ with wide band gap (1.60 eV) is closely in line with the experimental values ($\sim 1.45 \text{ eV}$) [16], which demonstrates the reliability of our calculations. In the PE and FE phases, the valence band maximum (VBM) is mostly occupied by the $\text{I}-5p_{x-y}$ orbitals, while the conduction band minimum (CBM) is mainly composed of $\text{Bi}-6p_z$ orbitals. These orbitals indicate that photogenerated electrons are likely to transition between Bi and I atoms. The VBM and CBM occupying different atoms can effectively inhibit the recombination of electron-hole pairs [68] and can improve energy storage efficiency [69]. Obviously, the band gap of FE phases is larger than that of PE phases, as shown in Figs. 4(a) and 4(b). Compared with the density of states (DOS) of PE phases, the CBM of FE phases are further away from the VBM, due to the fact that the bond lengths of Bi-I in the z direction are generally smaller than that of PE phases, as shown in Figs. 2(a) and 2(b). That is, the shorter distance between Bi and I atoms in the inorganic octahedron, the larger the band gap.

According to the previous analysis, the Bi atoms in the center of inorganic octahedrons play a key factor in the phase transition. Since the valence electrons of the Bi atom are composed of electrons of the $6s$ and $6p$ orbitals, it is necessary to further analyze these electrons during the phase transition. As shown in Figs. 4(a) and 4(b), there are two local peaks

of $\text{Bi}-6s^2$ near -10 eV , verifying the electronic $6s^2$ lone-pair stereoactivity of Bi^{3+} centers [13]. The partial charges near -10 eV of Bi atoms in the PE and FE phase display the strong localization, and no electron hybridization with other atoms was found [Figs. 4(c) and 4(e)]. This result reveals that the Bi^{3+} centers with a local electronic $6s^2$ lone pair are part of the FE displacement [50,70]. The $\text{I}-5p$ orbitals essentially hybridize with $\text{Bi}-6p$ orbitals on the valence band from -4 to 0 eV , as shown in Figs. 4(d) and 4(f). Between off-center Bi and I, atoms in the FE phase of the BiI_3Cl_2 octahedron possess stronger coupling of p - p orbitals than the PE phase. It can be deduced that the FE mechanism indeed originates from the strong p - p orbital coupling of $\text{I}-5p$ and off-center $\text{Bi}-6p$ in the BiI_3Cl_2 chains.

Furthermore, due to weak local characteristics of C, N, and H atoms compared with that of Bi and I atoms, the relatively wide energy range of hybridization among atoms of organic molecules for $(\text{MV})\text{BiI}_3\text{Cl}_2$ in the PE phase mainly exists from -10 to -5 eV . Compared with PE MV, the PDOS of FE MV only exhibits a small local change, implying that the displacement of MV organic molecules is not significant in this compound. The results agree well with our previous FE analysis in the Sec. III B.

In addition to band structural analysis, the optical absorption coefficients (α) of FE $(\text{MV})\text{BiI}_3\text{Cl}_2$ and $(\text{MV})\text{SbI}_3\text{Cl}_2$ are especially crucial for potential photovoltaic materials, as shown in Figs. 5(a) and 5(b), respectively. The optical absorption edges in the visible light range for $(\text{MV})\text{BiI}_3\text{Cl}_2$ and $(\text{MV})\text{SbI}_3\text{Cl}_2$ are well aligned with the aforementioned band gaps, respectively. We found that the optical absorption coefficient of $(\text{MV})\text{BiI}_3\text{Cl}_2$ in the visible light absorption is greater than that of $(\text{MV})\text{SbI}_3\text{Cl}_2$. The α value parallel to the c direction is much higher than that vertical to the c

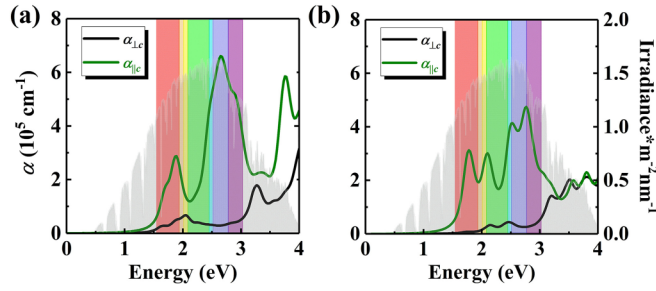


FIG. 5. The optical absorption coefficient α of ferroelectric (FE) phases in (a) (MV)BiI₃Cl₂ and (b) (MV)SbI₃Cl₂ along vertical and parallel to c axis. The AM 1.5G solar radiation spectrum (light gray) is taken from the National Renewable Energy Laboratory (NREL) Website [37].

direction, meaning that (MV)AlI₃Cl₂ possess anisotropic optical absorption properties. The optical absorption edges of FE (MV)BiI₃Cl₂ and (MV)SbI₃Cl₂ can reach up to 1.60 and 1.66 eV, respectively, which are competitive with the well-known OIHP photovoltaic compound (MA)PbI₃ (1.65 eV) [71]. The band gap of (MV)BiI₃Cl₂ is smaller than that of (MV)SbI₃Cl₂, which is due to the fact that the Bi-6s is higher in energy than the Sb-5s, and therefore, the band gap is narrower in Bi materials, as shown in Fig. S4 in the SM [40], which agrees well with reported BiSI ($E_g = 1.78$ eV) and SbSI ($E_g = 1.95$ eV) [70,72].

The photoelectric conversion efficiency is also one of the important performances in photovoltaic materials. Based on Eqs. (2)–(5), the maximum short-circuit current (J_{sc}), open-circuit voltage (V_{oc}), and maximum power conversion efficiency (η) were calculated and listed in the Table II. From Table II, the E_g of (MV)BiI₃Cl₂ is slightly smaller than that of (MV)SbI₃Cl₂, resulting in the J_{sc} of (MV)BiI₃Cl₂ being larger than that of (MV)SbI₃Cl₂, suggesting that J_{sc} was determined by E_g . When FF = 80%, the calculated η [$\sim 18.34\%$ for (MV)BiI₃Cl₂ and $\sim 18.22\%$ for (MV)SbI₃Cl₂] with E_{loss} of 0.7 is competitive with that of high-performance photovoltaic (MA)PbI₃ ($\eta \sim 18\%$) [71], which indicates these materials are potential candidates for perovskite solar cells.

High carrier mobility is an important performance criterion for optoelectronic and photovoltaic devices. The carrier mobility of (MV)AlI₃Cl₂ was theoretically calculated using the deformation potential theory [73], as shown in the following equation:

$$\mu = \frac{(8\pi)^{1/2} \hbar^4 C_{ij}}{3(m^*)^{5/2} (k_B T)^{3/2} E_1^2}, \quad (11)$$

TABLE II. Calculated parameters for FE phase (MV)BiI₃Cl₂ and (MV)SbI₃Cl₂ including band gap E_g (eV), the maximum short circuit current density J_{sc} (mA/cm²), open circuit voltages V_{oc} (V), and maximum power conversion efficiency η (%) with different loss-in-potential E_{loss} when FF is 80%. Exp. = experimental.

Material	E_g	J_{sc}	$V_{oc}(E_{loss} = 0.7 \text{ eV})$	$V_{oc}(E_{loss} = 0.5 \text{ eV})$	$\eta(E_{loss} = 0.7 \text{ eV})$	$\eta(E_{loss} = 0.5 \text{ eV})$
(MV)BiI ₃ Cl ₂	1.60	25.47	0.90	1.10	18.34	22.41
(MV)SbI ₃ Cl ₂	1.66	23.72	0.96	1.16	18.22	23.01
(MA)PbI ₃ [71]	1.65 (exp.)	~ 22.4 (exp.)	~ 0.92 (exp.)		~ 18 (exp.)	

where \hbar is the reduced Planck constant, e is the element charge, C_{ij} is the elastic matrix constant, m^* is the carrier effective mass, k_B is the Boltzmann constant, and T is temperature. Here, E represents the deformation potential constant of the VBM for hole or CBM for electron along the transport direction, defined by $E_1 = \Delta E/(\Delta l/l)$. Here, ΔE is the energy shift of the CBM or VBM under proper lattice compression or dilatation, l is the lattice constant in the transport direction, and Δl is the deformation of l . The temperature used for the mobility calculations was 300 K. Note that the carrier mobilities along different transport directions are calculated based on the unit cell of (MV)AlI₃Cl₂. According to Eq. (11), the effective mass, the elastic modulus, and the band deformation potential all contribute to carrier mobility. The effective mass plays the key role in the carrier mobility because its index ($\frac{5}{2}$) is larger than that of the other two variables. The difference of effective mass directly results in large different mobility. As shown in Table III, the smallest electronic effective mass of (MV)BiI₃Cl₂ along the z direction results in a larger electronic mobility ($7.49 \times 10^3 \text{ cm}^2 \text{ V}^{-1} \text{ s}^{-1}$), which is competitive with that of the high-performance orthorhombic OIHP CH₃NH₃PbI₃ ($8.30 \times 10^3 \text{ cm}^2 \text{ V}^{-1} \text{ s}^{-1}$) [74]. From Table III, we also note that the high electronic mobility in (MV)BiI₃Cl₂ along the z direction is ~ 4 orders of magnitude larger than that along the $x(y)$ direction. Such huge anisotropic electronic mobilities are very rare in the OIHP materials. On the contrary, the hole mobility of (MV)BiI₃Cl₂ along the $x(y)$ direction is much larger than that along the z direction, resulting from the different value of the effective mass of the hole on the VBM, which is originated from larger electronic density on the VBM between I atoms and Bi atoms along the $x(y)$ direction, as shown in Fig. S5(a) in the SM [40]. As shown in Table III, the effective mass of the holes in the Bi system is smaller than that of the Sb system along the $x(y)$ direction, due to strong interaction between Bi and I. As shown in Fig. S5 in the SM [40], the electron density between Bi and I atoms along the $x(y)$ direction is larger than that between Sb and I atoms. These results agree well with the previous paper that the BiI₃ monolayer has a significantly lower hole effective mass than that of the SbI₃ monolayer [75]. However, the electron density between Bi and I atoms along the z direction is smaller than that between Sb and I atoms, suggesting that the hole effective mass of the Bi system is larger than that of the Sb system, which is in line with the differences between bulk BiI₃ and SbI₃ [75]. Since the electrons and holes have different easy directions of movement in (MV)BiI₃Cl₂ along the z and x directions, respectively, strong electron and hole anisotropy enhances the separation of photogenerated electron-hole pairs [76]. In (MV)SbI₃Cl₂, the high electron (hole) carrier

TABLE III. Calculated carrier effective masses $m^*(m_0)$, elastic moduli C_{ij} (Gpa), deformation potentials E_1 (eV), and carrier mobility $\mu(\text{cm}^2 \text{V}^{-1} \text{s}^{-1})$ along $x(y)$ and z direction at $T = 300$ K. Ele. = electron.

Structure	Type	$m_{x(y)}^*/(m_0)$	$m_z^*/(m_0)$	$C_{x(y)}$ (Gpa)	C_z (Gpa)	$E_{1x(y)}$ (eV)	E_{1z} (eV)	$\mu_{x(y)}$ ($\text{cm}^2 \text{V}^{-1} \text{s}^{-1}$)	μ_z ($10^3 \text{cm}^2 \text{V}^{-1} \text{s}^{-1}$)
(MV)BiI ₃ Cl ₂	Ele.	15.69	0.12	22.21	26.04	5.68	6.55	0.04	7.49
	Hole	1.77	12.07	22.21	26.04	7.05	5.69	6.49	0.10×10^{-3}
(MV)SbI ₃ Cl ₂	Ele.	6.70	0.13	23.32	23.33	5.48	6.33	0.41	6.94
	Hole	3.24	0.50	23.32	23.33	7.26	6.81	1.42	0.17
CH ₃ NH ₃ PbI ₃ [74] (orthorhombic)	Ele.	0.26	0.18	26.7	44.3	1.49	4.89	21.6×10^3	8.30
	Hole	0.30	0.27	26.7	44.3	4.05	6.74	2.00×10^3	1.60

mobilities along the z direction are obviously four (two) orders of magnitude larger than that along the $x(y)$ direction, suggesting anisotropic carrier mobility. Moreover, in the z direction, the electron mobility is ~ 40 times that of the hole, indicating that this carrier mobility difference can also effectively enhance the separation of electron-hole pairs [77].

E. Strain engineering

Mechanical strain engineering is one of the methods to effectively modulate the material structure. Considering the polarization dependence on the c direction, we performed the strain engineering strategy to calculate electronic structures, FE polarization, optical absorption, and carrier mobility of (MV)AlI₃Cl₂ with uniaxial strain [$\varepsilon = (c - c_0)/c_0$] from -3% (compression) to 3% (stretching) along the c direction. The polarization of (MV)AlI₃Cl₂ with uniaxial strain along the c direction was calculated, as shown in Figs. 6(a) and 6(b). Using the theory of piezoelectricity, we found that the strain-induced change in polarization is mainly composed of (1) direct change in strain and (2) strain-induced change in polar lattice distortion. Generally, the relationship of strain and

dipole moment is shown in the following equation:

$$e_{33} = \frac{\partial}{\partial \varepsilon} (V^{-1} p)_{\varepsilon=0} = -\frac{p_0}{V_0} + \frac{1}{V_0} \frac{\partial p}{\partial \varepsilon} \Big|_{\varepsilon=0}$$

$$= -P_0 + \frac{1}{V_0} \frac{\partial p}{\partial \varepsilon} \Big|_{\varepsilon=0}, \quad (12)$$

where e_{33} , p_0 , and V_0 are the piezoelectric tensor in the c direction, dipole moment, and cell volume at $\varepsilon = 0$, respectively. The term P_0 represents the polarization of the material without strain, which is equivalent to the spontaneous polarization (P) discussed previously. In Eq. (12), the positive and negative values of the two terms are in a competitive relationship for the contribution to piezoelectric effects, as shown in Table I. The second term shows that the dipole moment is in an increasing trend with stretching volume. The magnitude of the first item is smaller than that of the second item, indicating that the deformation of polarization mainly comes from the dipole moment component of the strain-induced change. The larger second item means (MV)AlI₃Cl₂ can be easily controlled by external forces.

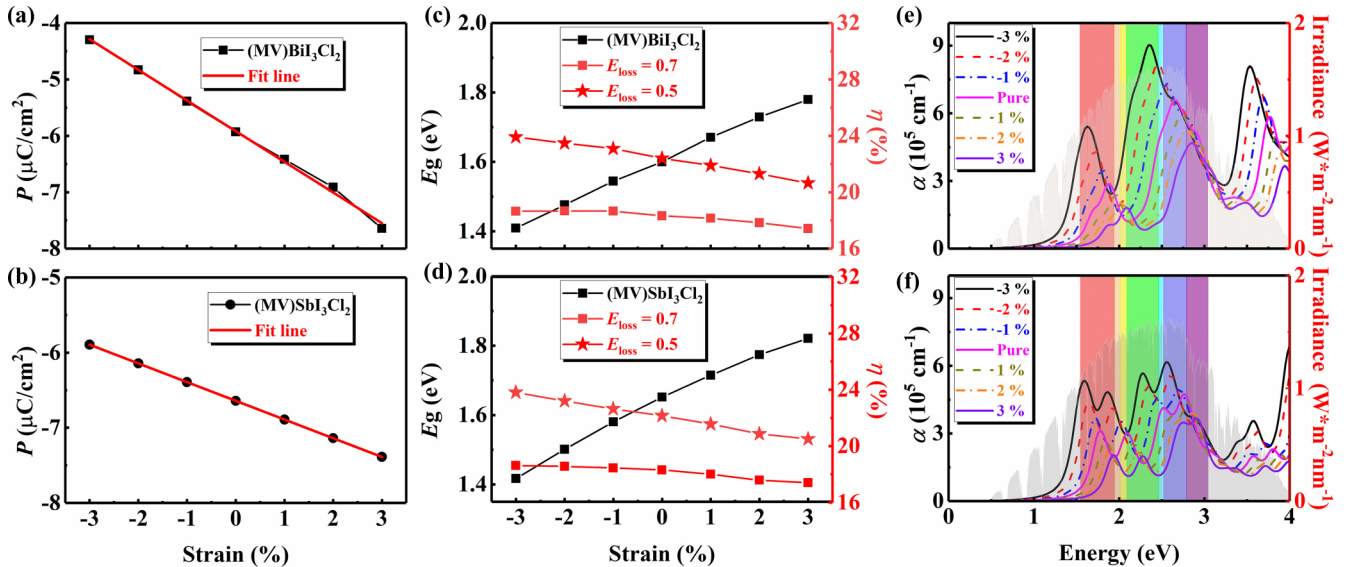


FIG. 6. Calculated polarization vs strain (ε) of (a) (MV)BiI₃Cl₂ and (b) (MV)SbI₃Cl₂ along the c direction. Red solid lines are fitting curves whose slopes at equilibrium ($\varepsilon = 0$, dashed vertical line) correspond to e_{33} in Table IV. The band gap (E_g) and maximum power conversion efficiency (η) in different loss-in-potential (E_{loss}) of 0.7 and 0.5 for (c) (MV)BiI₃Cl₂ and (d) (MV)SbI₃Cl₂ with applied strain ranging from -3% to 3% . The absorption coefficient (α) of (e) (MV)BiI₃Cl₂ and (f) (MV)SbI₃Cl₂ with applied strain ranging from -3% to 3% . The AM 1.5G solar radiation spectrum (light gray) is taken from National Renewable Energy Laboratory (NREL) Website [37].

TABLE IV. Calculated piezoelectric properties of (MV)BiI₃Cl₂ including elastic constants C_{ij} (GPa), piezoelectric stress coefficients e_{ij} (C/m²), and piezoelectric strain coefficients d_{ij} (pC/N).

Structure	C_{11}	C_{12}	C_{13}	C_{33}	C_{44}	C_{66}	e_{16}	e_{25}	e_{31}	e_{33}	d_{16}	d_{25}	d_{31}	d_{33}
(MV)BiI ₃ Cl ₂	22.21	20.25	20.09	26.04	3.43	8.94	0.035	0.035	0.047	0.540	3.9	10.2	-32.1	70.3
(MV)SbI ₃ Cl ₂	23.32	19.90	18.14	23.33	2.55	9.83	0.006	0.006	0.049	0.249	0.6	2.3	-9.7	25.7

It is known that piezoelectricity is the result of the electromechanical interaction, which is usually described by piezoelectric coefficients, i.e., piezoelectric tensors and piezoelectric strain tensors. The elastic matrix possesses six independent constants C_{ij} [78], and the piezoelectric stress tensor matrix possesses four independent coefficients e_{ij} [79]. The piezoelectric strain coefficient d_{ij} can be calculated as

$$d_{ij} = \sum_{k=1}^6 e_{ik} C_{kj}^{-1}. \quad (13)$$

Here, all piezoelectric coefficients are summarized in Table IV. The values of the elastic matrix constants C_{ij} all meet the Born stability criteria for the tetragonal $4mm$ class [78], as indicated in the following: (1) $C_{11} > |C_{12}|$, (2) $2C_{13}^2 < C_{33}(C_{11} + C_{12})$, and (3) $C_{44} > 0$. The key coefficients for piezoelectric performance d_{33} are 70.3 and 25.7 pC/N for (MV)BiI₃Cl₂ and (MV)SbI₃Cl₂, respectively, which are superior to the corresponding value of the classical piezoelectric ZnO ($d_{33} = 12.3$ pC/N) [80].

The band gap of the FE phase of (MV)AlI₃Cl₂ increases with strain from compression to stretching, as shown in Figs. 6(c) and 6(d). The band gap increases because the energy band width becomes narrower for Bi-6 p_z (Sb-5 p_z) of the CBM and I-5 p_{x-y} of the VBM (Fig. S6 in the SM [40]). Under

3% compression, the band gap of (MV)SbI₃Cl₂ is 1.42 eV, which is close to the ideal photovoltaic band gap of 1.4 eV of amorphous silicon and GaAs [81,82]. The optical absorption of (MV)AlI₃Cl₂ was affected by the structures upon strain engineering [Figs. 6(e) and 6(f)]. Firstly, the optical absorption peaks of all cases with strain from -3 to 3% are in the visible light range, ensuring sufficient solar absorption. Secondly, the first main absorption peaks for both samples gradually decrease with stretching. Then the maximum power conversion efficiency (η) of (MV)BiI₃Cl₂ and (MV)SbI₃Cl₂ also increases under the increase of applied compression. Therefore, at the loss-in-potential (E_{loss}) of 0.5, the η of (MV)BiI₃Cl₂ and (MV)SbI₃Cl₂ under the compression of 3% can reach 23.92 and 23.81%, respectively. The (MV)BiI₃Cl₂ and (MV)SbI₃Cl₂ with suitable compression methods can be a potential high-efficiency FE photovoltaic cell.

In realistic situations, strain engineering can be achieved during the film formation process or under applied mechanical force [83]. The most likely route of uniaxial strain is epitaxial growth on a substrate with controlled structural phase change contraction and expansion [84,85]. However, the strain effect can only exist on a film with a very thin interface, which may have little obvious effect on the light absorption. For application of strain effects on photovoltaic properties in these materials, multilayered structured film is preferred, which can enhance efficiency of optical absorption. On the other hand,

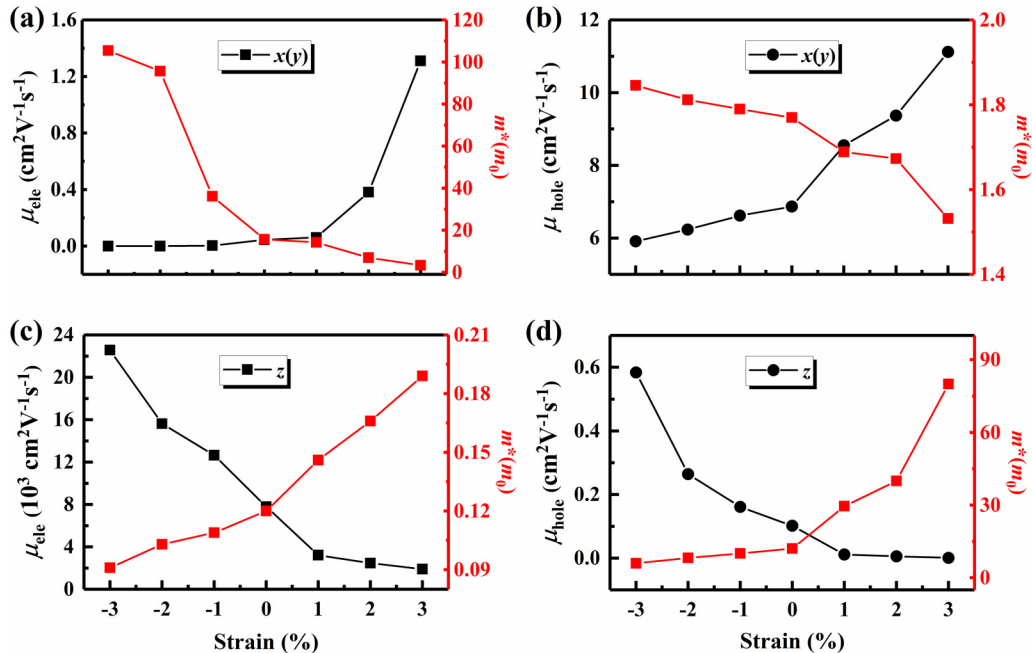


FIG. 7. The electron carrier mobility (μ_{ele}) and effective mass (m^*) in (MV)BiI₃Cl₂ along (a) $x(y)$ and (c) z directions. The hole carrier mobility (μ_{hole}) and effective mass (m^*) in (MV)BiI₃Cl₂ along (b) $x(y)$ and (d) z directions.

strain engineering can also be achieved by mechanical methods including hydrostatic pressurization [85–88].

The carrier mobility (μ) generally determines the migration length of the electron and hole. Because carrier mobilities of (MV)Bi₃Cl₂ and (MV)SbI₃Cl₂ originate from the Bi (Sb) and I atoms of inorganic perovskites, the wavelength of thermally activated charge carriers at room temperature is much larger than their lattice constant and is close to that of acoustic phonon mode [89,90]. The electron-acoustic phonon coupling dominates the scattering at the low energy regime [91,92], which can be described by the deformation potential theory [73]. In addition, the VBM and CBM of (MV)AlI₃Cl₂ with strain engineering are mainly contributed from inorganic octahedrons, as shown in Fig. S6 in the SM [40]. Hence, the carrier mobility of strain engineering was also calculated by the deformation potential theory.

The carrier mobility is changed under strain engineering from -3 to 3% , as shown in Fig. 7. Applying strain to the (MV)Bi₃Cl₂ systems, the electron and hole mobility along the $x(y)$ directions are in increasing trend under stretching, as shown in Figs. 7(a) and 7(b). However, the electron and hole mobility along the z direction are in decreasing trend [Figs. 7(c) and 7(d)]. The different trend of carriers in different directions leads to an enhancement of anisotropy. This phenomenon mainly originates from the fact that the carrier mobility under strain is opposite to the change of effective mass. On the other hand, high electron mobility ($2.26 \times 10^4 \text{ cm}^2 \text{ V}^{-1} \text{ s}^{-1}$) in the z direction is larger than the carrier mobility of typical OIHP CH₃NH₃GeI₃ of $1.35 \times 10^3 \text{ cm}^2 \text{ V}^{-1} \text{ s}^{-1}$ [93]. Comparing the (MV)Bi₃Cl₂ systems, the carrier mobilities of (MV)SbI₃Cl₂ (Fig. S7 in the SM [40]) show similar increasing and decreasing trends along the

$x(y)$ and z directions, respectively. However, in the z direction, the hole mobility of (MV)SbI₃Cl₂ is about three times the order of magnitude than that of (MV)Bi₃Cl₂, suggesting that (MV)SbI₃Cl₂ in the z direction possesses considerable electron and hole mobility.

IV. CONCLUSIONS

Based on first-principles calculations with DFT, the mechanical, FE, optical, and electric properties of (MV)Bi₃Cl₂ and (MV)SbI₃Cl₂ have been systematically investigated. We found that, firstly, (MV)Bi₃Cl₂ and (MV)SbI₃Cl₂ are mechanically stable materials. Secondly, (MV)Bi₃Cl₂ and (MV)SbI₃Cl₂ possess robust spontaneous polarization. In addition, (MV)Bi₃Cl₂ with relatively low energy barrier between FE and AFE phase is suitable to be applied in memory devices. Thirdly, the strong optical absorption and high anisotropic carrier mobility of (MV)Bi₃Cl₂ and (MV)SbI₃Cl₂ can enhance the efficiency of solar energy utilization. Finally, application of uniaxial compression along the z direction of (MV)Bi₃Cl₂ and (MV)SbI₃Cl₂ enhance these materials with robust FE polarization, effective strong optical absorption, high power conversion efficiency, and large electric mobility, allowing them to be candidates for FE photovoltaic applications.

ACKNOWLEDGMENTS

This paper was partially funded by the National Natural Science Foundation of China (Grant No. 51572193) and the Natural Science Foundation of Tianjin (Grant No. 20JCZDJC00210).

-
- [1] C. Sun, L. Xu, X. Lai, Z. Li, and M. He, *Energ. Environmen. Mater.* **4**, 293 (2020).
- [2] B. Hwang and J.-S. Lee, *Adv. Electron. Mater.* **5**, 1800519 (2019).
- [3] P. Nandi, D. Topwal, N.-G. Park, and H. Shin, *J. Phys. D Appl. Phys.* **53**, 493002 (2020).
- [4] X. Xiao, J. Hu, S. Tang, K. Yan, B. Gao, H. Chen, and D. Zou, *Adv. Mater. Technol.* **5**, 1900914 (2020).
- [5] Z. Shi, J. Guo, Y. Chen, Q. Li, Y. Pan, H. Zhang, Y. Xia, and W. Huang, *Adv. Mater.* **29**, 1605005 (2017).
- [6] Y. Zhao and K. Zhu, *Chem. Soc. Rev.* **45**, 655 (2016).
- [7] H. W. Huang, H. F. Yuan, K. P. F. Janssen, G. S. Fernández, Y. Wang, C. Y. X. Tan, D. Jonckheere, E. Debroye, J. L. Long, J. Hendrix, J. Hofkens, J. A. Steele, and M. B. J. Roeflaers, *ACS Energy Lett.* **3**, 755 (2018).
- [8] C. Gu and J. S. Lee, *ACS Nano* **10**, 5413 (2016).
- [9] M. Sessolo and H. J. Bolink, *Adv. Mater.* **23**, 1829 (2011).
- [10] F. Sahli, J. Werner, B. A. Kamino, M. Bräuninger, R. Monnard, B. P. Salomon, L. Barraud, L. Ding, J. J. Diaz Leon, D. Sacchetto, G. Cattaneo, M. Despeisse, M. Boccard, S. Nicolay, Q. Jeangros, B. Niesen, and C. Ballif, *Nat. Mater.* **17**, 820 (2018).
- [11] W. S. Yang, B. W. Park, E. H. Jung, N. J. Jeon, Y. C. Kim, D. U. Lee, S. S. Shin, J. Seo, E. K. Kim, J. H. Noh, and S. I. Seok, *Science* **356**, 1376 (2017).
- [12] E. J. Yoo, M. Lyu, J. H. Yun, C. J. Kang, Y. J. Choi, and L. Wang, *Adv. Mater.* **27**, 6170 (2015).
- [13] N. Leblanc, N. Mercier, L. Zorina, S. Simonov, P. Auban-Senzier, and C. Pasquier, *J. Am. Chem. Soc.* **133**, 14924 (2011).
- [14] Y. Lei, S. Wang, S. Ma, Y. Shi, D. Fu, and W. Liu, *Appl. Phys. Lett.* **114**, 182902 (2019).
- [15] N. Leblanc, N. Mercier, M. Allain, O. Toma, P. Auban-Senzier, and C. Pasquier, *J. Solid State Chem.* **195**, 140 (2012).
- [16] J. Wang, J. Zheng, S. T. Wang, J. Sun, Y. M. Guo, H. Wang, S. G. Huang, Y. D. Li, and C. C. Wang, *Mater. Lett.* **254**, 419 (2019).
- [17] Y. H. Wen, H. B. Peng, D. Raabe, I. Gutierrez-Urrutia, J. Chen, and Y. Y. Du, *Nat. Commun.* **5**, 4964 (2014).
- [18] J. E. Lee, G. Ahn, J. Shim, Y. S. Lee, and S. Ryu, *Nat. Commun.* **3**, 1024 (2012).
- [19] N. T. Woodward, N. Nepal, B. Mitchell, I. W. Feng, J. Li, H. X. Jiang, J. Y. Lin, J. M. Zavada, and V. Dierolf, *Appl. Phys. Lett.* **99**, 122506 (2011).
- [20] K. J. Choi, M. Biegalski, Y. L. Li, A. Sharan, J. Schubert, R. Uecker, P. Reiche, Y. B. Chen, X. Q. Pan, V. Gopalan, L.-Q. Chen, D. G. Schlom, and C. B. Eom, *Science* **306**, 1005 (2004).
- [21] S. Ghosh, D. Di Sante, and A. Stroppa, *J. Phys. Chem. Lett.* **6**, 4553 (2015).
- [22] G. V. Sin'ko and N. A. Smirnov, *J. Phys. Condens. Mat.* **14**, 6989 (2002).

- [23] G. Kresse and J. Furthmüller, *Phys. Rev. B* **54**, 11169 (1996).
- [24] G. Kresse and J. Furthmüller, *Comp. Mater. Sci.* **6**, 15 (1996).
- [25] J. P. Perdew, K. Burke, and M. Ernzerhof, *Phys. Rev. Lett.* **77**, 3865 (1996).
- [26] J. Heyd, G. E. Scuseria, and M. Ernzerhof, *J. Chem. Phys.* **118**, 8207 (2003).
- [27] J. Heyd, G. E. Scuseria, and M. Ernzerhof, *J. Chem. Phys.* **124**, 219906 (2006).
- [28] R. D. King-Smith and D. Vanderbilt, *Phys. Rev. B* **47**, 1651 (1993).
- [29] G. Henkelman, B. P. Uberuaga, and H. Jónsson, *J. Chem. Phys.* **113**, 9901 (2000).
- [30] Bilbao Crystallographic Server, <http://www.cryst.ehu.es>
- [31] U.-G. Jong, C.-J. Yu, J.-S. Ri, N.-H. Kim, and G.-C. Ri, *Phys. Rev. B* **94**, 125139 (2016).
- [32] W. Shockley and H. J. Queisser, *J. Appl. Phys.* **32**, 510 (1961).
- [33] H. J. Snaith, *Adv. Funct. Mater.* **20**, 13 (2010).
- [34] M. R. Filip, C. Verdi, and F. Giustino, *J. Phys. Chem. C* **119**, 25209 (2015).
- [35] S. Rühle, *Sol. Energy* **130**, 139 (2016).
- [36] D. Liu, Q. Li, J. Hu, H. Jing, and K. Wu, *J. Mater. Chem. C* **7**, 371 (2019).
- [37] The AM 1.5G solar radiation spectrum, <https://www.nrel.gov/grid/solar-resource/spectra-am1.5.html>
- [38] G. Kieslich, S. Sun, and A. K. Cheetham, *Chem. Sci.* **5**, 4712 (2014).
- [39] G. Kieslich, S. Sun, and A. K. Cheetham, *Chem. Sci.* **6**, 3430 (2015).
- [40] See Supplemental Material at <http://link.aps.org/supplemental/10.1103/PhysRevB.104.075138> for optimization structures with different van der Waals interaction and k -points, which includes Refs. [13,15]; FE polarization with different k -points; partial and total polarization of (MV)Sb₃Cl₂; the DOS and charge density of PE and FE phases in the (MV)Sb₃Cl₂; band structure of (MV)Bi₃Cl₂ and (MV)Sb₃Cl₂ with HSE06 functional including spin-orbit coupling; PDOS of different atoms for (MV)Bi₃Cl₂ and (MV)Sb₃Cl₂; partial charge density of VBM for (MV)Bi₃Cl₂ and (MV)Sb₃Cl₂; PDOS of (MV)Bi₃Cl₂ and (MV)Sb₃Cl₂ under strain engineering; and carrier mobility and effective mass of (MV)Sb₃Cl₂ along different directions under strain engineering.
- [41] S. Grimme, *J. Comput. Chem.* **27**, 1787 (2006).
- [42] S. Grimme, J. Antony, S. Ehrlich, and H. Krieg, *J. Chem. Phys.* **132**, 154104 (2010).
- [43] J. Klimes, D. R. Bowler, and A. Michaelides, *J. Phys. Condens. Matter.* **22**, 022201 (2010).
- [44] C. Capillas, E. S. Tasci, G. de la Flor, D. Orobengoa, J. M. Perez-Mato, and M. I. Aroyo, *Z. Kristallogr.* **226**, 186 (2011).
- [45] Y. Lei, S. Wang, J. Xing, H. Xu, J. Han, and W. Liu, *Inorg. Chem.* **59**, 4349 (2020).
- [46] D. Orobengoa, C. Capillas, M. I. Aroyo, and J. M. Perez-Mato, *J. Appl. Crystallogr.* **42**, 820 (2009).
- [47] J. M. Perez-Mato, D. Orobengoa, and M. I. Aroyo, *Acta Crystallogr. A* **66**, 558 (2010).
- [48] N. A. Spaldin, *J. Solid State Chem.* **195**, 2 (2012).
- [49] W. P. Zhao, C. Shi, A. Stroppa, D. Di Sante, F. Cimpoesu, and W. Zhang, *Inorg. Chem.* **55**, 10337 (2016).
- [50] R. Jakubas, A. Piecha, A. Pietraszko, and G. Bator, *Phys. Rev. B* **72**, 104107 (2005).
- [51] K. Miura, T. Furuta, and H. Funakubo, *Solid State Commun.* **150**, 205 (2010).
- [52] V. Sharma, G. Pilania, G. A. Rossetti, K. Slenes, and R. Ramprasad, *Phys. Rev. B* **87**, 134109 (2013).
- [53] Y. Ma, B. Liu, Y. Zhou, and J. Ding, *Appl. Phys. Lett.* **96**, 122904 (2010).
- [54] A. Stroppa, C. Quarti, F. De Angelis, and S. Picozzi, *J. Phys. Chem. Lett.* **6**, 2223 (2015).
- [55] W. Bi, N. Leblanc, N. Mercier, P. Auban-Senzier, and C. Pasquier, *Chem. Mater.* **21**, 4099 (2009).
- [56] A. Piecha, A. Białońska, and R. Jakubas, *J. Mater. Chem.* **22**, 333 (2012).
- [57] T. E. Smidt, S. A. Mack, S. E. Reyes-Lillo, A. Jain, and J. B. Neaton, *Sci. Data* **7**, 72 (2020).
- [58] J. B. Neaton, C. Ederer, U. V. Waghmare, N. A. Spaldin, and K. M. Rabe, *Phys. Rev. B* **71**, 014113 (2005).
- [59] S. Hu, H. Gao, Y. Qi, Y. Tao, Y. Li, J. R. Reimers, M. Bokdam, C. Franchini, D. D. Sante, A. Stroppa, and W. Ren, *J. Phys. Chem. C* **121**, 23045 (2017).
- [60] H. Y. Zhang, Z. X. Zhang, X. J. Song, X. G. Chen, and R. G. Xiong, *J. Am. Chem. Soc.* **142**, 20208 (2020).
- [61] L. D. Filip, N. Plugaru, and L. Pintilie, *Modelling Simul. Mater. Sci. Eng.* **27**, 045008 (2019).
- [62] R. Fei, W. Kang, and L. Yang, *Phys. Rev. Lett.* **117**, 097601 (2016).
- [63] M. Zhao, G. Gou, X. Ding, and J. Sun, *Nanoscale* **12**, 12522 (2020).
- [64] S. Kim, V. Gopalan, and A. Gruverman, *Appl. Phys. Lett.* **80**, 2740 (2002).
- [65] S. Liu, I. Grinberg, and A. M. Rappe, *Nature (London)* **534**, 360(2016).
- [66] M. Ye and D. Vanderbilt, *Phys. Rev. B* **93**, 134303 (2016).
- [67] A. Onoe, S. Hashimoto, and Y. Cho, *Mater. Sci. Eng. B* **120**, 130 (2005).
- [68] W. H. Zhou, S. Y. Guo, S. L. Zhang, Z. Zhu, S. Y. A. Yang, M. X. Chen, B. Cai, H. Z. Qu, and H. B. Zeng, *Phys. Rev. Appl.* **11**, 064045 (2019).
- [69] C. S. Ponseca, Jr., P. Chabera, J. Uhlig, P. Persson, and V. Sundstrom, *Chem. Rev.* **117**, 10940 (2017).
- [70] A. M. Ganose, K. T. Butler, A. Walsh, and D. O. Scanlon, *J. Mater. Chem. A* **4**, 2060 (2016).
- [71] W. Y. Nie, H. Tsai, R. Asadpour, J. C. Blancon, A. J. Neukirch, G. Gupta, J. J. Crochet, M. Anish Chhowalla, S. Tretiak, M. A. Alam, H. L. Wang, and A. D. Mohite, *Science* **347**, 522 (2015).
- [72] K. T. Butler, S. McKechnie, P. Azarhoosh, M. van Schilfgaarde, D. O. Scanlon, and A. Walsh, *Appl. Phys. Lett.* **108**, 112103 (2016).
- [73] J. Bardeen and W. Shockley, *Phys. Rev.* **80**, 72 (1950).
- [74] Y. Wang, Y. Zhang, P. Zhang, and W. Zhang, *Phys. Chem. Chem. Phys.* **17**, 11516 (2015).
- [75] P. Liu, F. Lu, M. Wu, X. G. Luo, Y. H. Cheng, X. W. Wang, W. C. Wang, W. H. Wang, H. Liu, and K. Cho, *J. Mater. Chem. C* **5**, 9066 (2017).
- [76] W. Zhou, N. Umezawa, R. Z. Ma, N. Sakai, Y. Ebina, K. Sano, M. J. Liu, Y. Ishida, T. Aida, and T. Sasaki, *Chem. Mater.* **30**, 6449 (2018).
- [77] J. S. Qiao, X. H. Kong, Z. X. Hu, F. Yang, and W. Ji, *Nature Commun.* **5**, 4475 (2014).

- [78] F. Mouhat and F. X. Coudert, *Phy. Rev. B* **90**, 224104 (2014).
- [79] M. de Jong, W. Chen, H. Geerlings, M. Asta, and K. A. Persson, *Sci. Data* **2**, 150053 (2015).
- [80] X. Wu, D. Vanderbilt, and D. R. Hamann, *Phys. Rev. B* **72**, 035105 (2005).
- [81] T. Zdanowicz, T. Rodziewicz, and M. Zabkowska-Waclawe, *Solar Energy Mater. Solar Cells* **87**, 757 (2005).
- [82] W. J. Yin, T. Shi, and Y. Yan, *Adv. Mater.* **26**, 4653 (2014).
- [83] E. G. Moloney, V. Yeddu, and M. I. Saidaminov, *ACS Mater. Lett.* **2**, 1495 (2020).
- [84] N. Rolston, K. A. Bush, A. D. Printz, A. Gold-Parker, Y. Ding, M. F. Toney, M. D. McGehee, and R. H. Dauskardt, *Adv. Energy Mater.* **8**, 1802139 (2018).
- [85] J. J. Zhao, Y. H. Deng, H. T. Wei, X. P. Zheng, Z. H. Yu, Y. C. Shao, J. E. Shield, and J. S. Huang, *Sci. Adv.* **3**, eaao5616 (2017).
- [86] M. Li, T. Liu, Y. Wang, W. Yang, and X. Lü, *Matter Radiat. Extrem.* **5**, 018201 (2020).
- [87] S. Liu, S. S. Sun, C. K. Gan, A. G. Águila, Y. N. Fang, J. Xing, T. T. H. Do, T. J. White, H. G. Li, W. Huang, and Q. H. Xiong, *Sci. Adv.* **5**, eaav9445 (2019).
- [88] D. Ghosh, A. Aziz, J. A. Dawson, A. B. Walker, and M. S. Islam, *Chem. Mater.* **31**, 4063 (2019).
- [89] Y. Cai, G. Zhang, and Y. W. Zhang, *J. Am. Chem. Soc.* **136**, 6269 (2014).
- [90] M. Soleimani and M. Pourfath, *Nanoscale* **12**, 22688 (2020).
- [91] J. H. Lee, Z. Deng, N. C. Bristowe, P. D. Bristowe, and A. K. Cheetham, *J. Mater. Chem. C* **6**, 12252 (2018).
- [92] K. Huang, K. Lai, C. L. Yan, and W. B. Zhang, *J. Chem. Phys.* **147**, 164703 (2017).
- [93] Y. Q. Zhao, B. Liu, Z. L. Yu, J. Ma, Q. W. Qiang Wan, P. B. He, and M. Q. Cai, *J. Mater. Chem. C* **5**, 5356 (2017).